

Supplementary information for Projecting urban land expansion and heat island intensification globally through 2050

Two models are built and integrated to project urban heat island (UHI) intensification globally: 1) a spatially explicit, probabilistic urban expansion model to predict the likelihood of a location to convert to urban land, and 2) a sigmoid-based, two-step empirical model to relate UHI intensities to urban cluster size. Applying these two models on the Shared Socioeconomic Pathways(1, 2), we project how several plausible development scenarios will result in urban land expansion and heat island intensification through 2050 across the world.

1 Urban land expansion projections

The urban expansion model is built upon a previous global forecast model, URBANMOD(3), which first predicts the amounts of urban land then allocates them spatially with 5-km resolution. We develop a new forecast model, called URBANMOD-ZIPF, whose name indicates that Zipf's law of urban size distribution is preserved. Zipf's law refers to the linear and inverse relationship between ranks and sizes of cities on log scales(4). Since UHI intensity increases with log urban size(5–8), without preserving the Zipf's law in the forecasts, we cannot reliably predict the log size-dependent UHI. To develop URBANMOD-ZIPF, we significantly modify both the quantity prediction and land allocation processes of URBANMOD.

1.1 Delineating urban land

We use the Global Human Settlement Layer(9) (GHSL) datasets to delineate existing urban lands. By combining images from multiple satellite-born sensors, GHSL maps global human settlements in four years: 1975, 1990, 2000, and 2015. The global and multi-year coverage allows us to build and validate our urban expansion model across the world. GHSL provides three types of products, including built-up (GHS-BUILT), population (GHS-POP), and cities (GHS-SMOD). Among these three types of products, we choose GHS-SMOD as the delineation of urban lands, because it combines impervious surface and population density, which are the two most commonly used criteria to define urban area. The GHS-SMOD is resampled from the original 1-km resolution to 5-km used in URBANMOD-ZIPF.

1.2 Forecasting urban land quantities

This first improvement of URBANMOD-ZIPF over URBANMOD is the use of fixed effect panel data regression.

According to a previous meta-analysis(10) on drivers of global urban land expansion, the growth of gross domestic production (GDP) is the most significant factor. However, the patterns of how GDP drives urban expansion can vary across different regions of the world. To account for the regional variation, we build a fixed-effect panel data regression model to capture the relationship between per capita urban land and GDP. This regression model was not applicable when URBANMOD was developed, because only one year of global urban extents—the MODIS global urban cover in 2000 was available.

The panel data regression is built on historical observations in 1975, 1990, and 2000:

$$ULC_{it} = \beta_0 + \beta_1 GDC_{it} + \sum_{j=2}^N \gamma_j D_{ij} + \varepsilon_{it}$$

where β_0 is a constant, β_1 is the coefficient of GDC and URB, γ_j is the coefficient of the regional dummies D_{ij} , ε_{it} is the error term, N is the number of regions, and t represents the year. Supplementary Table 2 shows the estimates of coefficients in the regression. The panel regression ($R^2 = 0.94$) agrees better with observations than the simple linear regression ($R^2 = 0.34$). The simple regression overestimates ULC for regions with less than 200 km² while underestimates that for regions with more than 400 km², which are corrected in the panel data regression. Applying this equation on the future GDC in SSPs, we can estimate the future ULC by 2050. By multiplying per capita urban land with the urban population, we can forecast the future urban land in each region under each scenario.

Supplementary Table 4 shows the new urban lands forecasted here, from 2015 to 2050, and those by Seto et al. 2012 (3), from 2000 to 2030. Although these two methods span across different time periods and scenarios, we can still see that they forecast comparable amounts of urban lands in America, Europe and Oceania, but URBANMOD-ZIPF forecasts much less in Africa and Asia. That is because the fixed-effect regression used in URBANMOD-ZIPF can account for regional differences: African and Asian countries tend to have denser cities, thus smaller urban land per capita, than American, European and Oceanian countries. This is reflected in Supplementary Table 2, where Asian and African countries/regions have smaller coefficients (γ_j) of the regional dummies.

1.3 Forecasting urban land locations

The second improvement of URBANMOD-ZIPF over URBANMOD is the mechanism to preserve the Zipf's law of urban size distribution.

In terms of allocating urban land spatially, URBANMOD uses a spatially explicit grid-based model, based on urban development suitability derived from slope, distance to roads, population density, and land cover. Here in URBANMOD-ZIPF, we modify the allocation process by preserving the Zipf's law of urban size distribution. Considering the observation that Zipf's law is preserved because the expansion magnitude of an urban cluster is proportional to its size(4), we alter the probability of a grid converting to urban by multiplying the conversion probability by the size of the adjacent urban cluster. If multiple clusters are merged, the size of the new cluster will be used in the next iteration. Supplementary Figure 3 shows the rank-size distributions of urban clusters forecasted by URBANMOD-ZIPF (black) and URBANMOD (blue), and those from the GHSL datasets in 1975 (green), 1990 (yellow), 2000 (orange), and 2015 (red). As can be seen from the figure, URBANMOD-ZIPF is capable of preserving the historical rank-size distribution of urban clusters, while URBANMOD tends to underestimate the sizes of larger clusters.

1.4 Validating and comparing urban expansion projections

We use the observed urban land cover in 2015 to validate the accuracies of these two models. In land use change modelling, accuracy should be measured as the comparison between predicted and observed changes(11). Therefore, we first run both models from 2000 to 2015, then overlap the results with the new urban lands observed during the same period. If the model is more accurate in predicting land use changes, it should predict higher probabilities on the actual new urban lands. Supplementary Table 3 shows the average probabilities predicted by two models on the new urban lands from 2000 to 2015. In terms of predicting higher probabilities on observed

new urban lands, URBANMOD-ZIPF outperforms URBANMOD by 72%. Supplementary Figure 4 shows the predicted probabilities on urban clusters of various sizes. Regarding urban cluster sizes, URBANMOD-ZIPF outperforms URBANMOD in predicting clusters that are larger than 130 km² but underperforms in predicting clusters smaller than 130 km².

Another commonly used metric to validate probabilistic forecasts is to calculate the root-mean-square-error (RMSE) between the observed frequency and the predicted probabilities(12). First, we divide the predicted probabilities into ten equal size intervals. Then, we estimate the frequency of observed new urban lands from 2000 to 2015 within each interval. Finally, the RMSE between observed frequencies and predicted probabilities of these intervals are calculated. As shown in Supplementary Table 3, by this measure, URBANMOD-ZIPF achieves about 20% smaller RMSE compared to URBANMOD.

2 Urban heat island intensification projections

Two types of urban heat island (UHI) indicators are commonly used in urban climate studies: the atmospheric UHI (AUHI) and surface UHI (SUHI). The AUHI is based on air temperature, which can be measured by thermometers, which are installed sparsely in most cities worldwide; while the SUHI is based on land surface temperature, which can be measured continuously across the space by radiometers onboard satellites or aircraft. Here, we build two models to predict SUHI and AUHI respectively. Taking advantage of the spatially continuous measurements, the first model links SUHI to urban cluster size, while controlling other UHI determinants. The second model links air temperature to land surface temperature, in order to convert the estimated SUHI to AUHI.

2.1 Measuring surface urban heat island and its determinants

We measure SUHIs with the MOD11A2 land surface temperature (LST) 8-day product derived from the images obtained by the Moderate Resolution Imaging Spectroradiometer (MODIS) instrument on board the Terra satellite. The approach by (13) is used to fill the gaps in these images due to cloud coverage. Following (6, 8, 14, 15), we measure the SUHI as the difference between the mean LST of an urban cluster and its equal-area buffer zone. Before calculating SUHI, water pixels are removed from both the urban clusters and the buffer zones, and urban pixels are removed from the buffer zones.

To account for the diurnal, seasonal and intra-urban variations of urban heat islands, we define different types of SUHIs and build separate models respectively. For diurnal variation, we measure SUHIs with the daytime and nighttime LSTs from MOD11A2, which are obtained by Terra satellite at ~10:30 and at ~22:30 local solar time. We choose MOD11A2 from Terra rather than MYD11A2 from Aqua, because the former shows a better correlation with daily maximum and minimum air temperature (see session 2.3 for more details). For seasonal variation, we measure the summer and winter SUHIs with LSTs in Jun to August and December to February in the northern hemisphere (opposite months in the southern hemisphere). For intra-urban variation, we first classify the LSTs in an urban cluster into four quantiles (0-25th, 25-50th, 50-75th and 75-100th percentiles) and then measure SUHI of each quantile as the difference between its mean LST from that of the buffer zone. These LST quantiles each represent zones within an urban cluster that have different UHI intensities, usually ranging from the hottest center zone (75th–100th) to the coolest outskirts (0th–25th). In total, there are 16 types of SUHIs as listed in Supplementary Table 5.

We use other remote sensing products to measure the known determinants of SUHI in the existing large-scale studies:

- 1) Urban cluster size(6–8, 14, 16, 17): measured as the area of urban clusters delineated from GHSL using the City Clustering Algorithm(18);
- 2) Urban cluster compactness(14, 19): measured as the ratio between areas of the cluster and its minimum circumscribed circle;
- 3) Vegetation abundance(15, 19): approximated by the difference of the mean Enhanced Vegetation Index (EVI) between the cluster and its buffer zone, using the MYD13A1 product;
- 4) Surface albedo(15, 16, 20): approximated by the difference of mean white sky albedo between the cluster and its buffer zone, using the MCD43B3 product;
- 5) Surface roughness(20): approximated by the mean difference of backscattering between the cluster and its buffer zone, using the VV and VH composites of Sentinel-1 SAR data;
- 6) Anthropogenic heat(15, 16): approximated by the VIIRS Stray Light Corrected Nighttime product.

All variables are measured in 2015, because this is the only year when both GHSL and MODIS datasets are available. Among these determinants, anthropogenic heat has a stronger influence over AUHI than SUHI, and its diurnal and seasonal profiles vary in different regions across the world, which cannot be adequately captured here. The anthropogenic heat release depends on energy, transportation, built infrastructures and human activities, whose future changes are not explicitly modeled in the projections of urban land expansion. Therefore, we leave out the influences of changing anthropogenic heat in our models and only focus on the effects of urban expansion.

2.2 Modeling surface urban heat island

We build a sigmoid-based regression model to predict how SUHIs will intensify as urban clusters grow larger in size, while other determinants stay constant. We first transform urban cluster size with sigmoid functions then use multiple linear regression to model the SUHI as a function of sigmoid-transformed size and other determinants.

Although previous studies suggest positive relationships between SUHI and urban cluster size, there is a considerable discrepancy in the literature. While Li et al. (2017) (8) and Tan & Li (2015) (7) found linear relationships between SUHI and logarithmic urban cluster size in the continental U.S. and North China, Zhou et al. (2013) (6) found a non-linear, sigmoid relationship in Europe. Here, we replicate the analysis at the global scale by binning urban clusters according to their logarithmic sizes and calculating the average SUHIs of each bin. Replicating the analysis at the global scale allows sufficient sample sizes to more reliably test the underlying relationship between urban size and UHI. Supplementary Figure 5 shows the results for the 75-100th percentiles SUHIs during daytime and nighttime, in summer and winter. The binning analysis suggests non-linear sigmoid relations at the global scale across different seasons and time of day. The binning analyses for all four quantiles are shown in Supplementary Figure 6, where only the SUHIs of 0-25th percentiles do not increase with logarithmic size. After fitting the sigmoid functions S^* :

$$SUHI = S(\log_{10}(\text{size})) = \frac{a}{1 + (\log_{10}(\text{size})/b)^{-c}}$$

with the binning average on different types of SUHIs, we apply these functions to the logarithmic urban sizes, in order to obtain sigmoid size indices that are linearly correlated to

SUHIs. We create the sigmoid size indices for all types of SUHIs except those of 0-25th percentiles, because they are not correlated with size. Supplementary Table 5 shows the correlations between urban cluster $\log_{10}(\text{size})$, sigmoid size indices $S(\log_{10}(\text{size}))$, and SUHIs. As shown in the table, the sigmoid size indices have stronger linear correlations with SUHIs. This transformation allows for the multiple regression that assumes linearity.

To demonstrate the significance of urban cluster size in determining SUHIs, we run the best subsets regressions(21) between SUHIs of 75-100th percentiles and the determinants listed in 2.1. The best subsets regression compares all possible combinations of independent variables, in order to find the best subset of variables that yields the highest coefficient of determination (R^2). Supplementary Table 6 shows the summary of the best subsets sorted by the resulting R^2 . Our analyses show that, compared to other determinants, the sigmoid size indices ($S(\log_{10}(\text{size}))$) of urban clusters contribute the most to correlations (from 79% to 94%) with all types of SUHIs and therefore they are the suitable variables in predicting future SUHIs.

Previous studies(8, 20, 22) suggest that SUHIs are influenced by the climatic-ecological contexts, which are accounted for by building conditional linear regressions. Specifically, we build separate models for urban clusters within different Köppen-Geiger climate zones(23): the arid, cold, temperate and tropical. The summaries of these regression models are shown in Supplementary Table 7, where the coefficients of determination (R^2) are higher than 0.7 except for winter nighttime. Note that in the arid climate, only the SUHIs of 75-100th percentiles increase with size while those of the other two quantiles decrease. In arid climate, although dense development in the urban cores increases the temperature, the urban green spaces introduced in the less dense areas actually cool down the surface. This is consistent with previous studies that found urban cool islands(24, 25) in the arid zones.

2.3 Predicting air temperature with the land surface temperature

Although it is possible to measure and model SUHI at the global scale, predicting future SUHI intensification is less useful because the impacts of warming on human health and energy consumption are more relevant to air temperature. Here, we build a model to predict daily maximum and minimum air temperature (AT) from daytime and nighttime LST, based on a series of methods developed and tested in diverse regions such as the U.S.(26–29), China(30–32), Europe(33, 34), the Middle East(35) and Africa(36). The daily maximum and minimum air temperatures used here are obtained from the Global Historical Climatology Network-Daily (GHCN-D) dataset version-3 (37), which include over 80,000 weather stations in 180 countries and territories. To avoid the influences of rural stations, we spatially overlay the GHCN stations with GHSL urban extent in 2015, to identify 1,074 urban stations to be used in the regression (Supplementary Figure 7).

The air temperature (AT) is modeled as:

$$AT = (\beta_0 + \beta_1 \times LST + \beta_2 \times elev + \beta_3 \times d_{water} | c_i)$$

where $elev$ is the elevation, d_{water} is the distance to the closest water body, and c_i denotes the climatic zone.

In the previous regional AT-LST modeling studies, both LSTs of MOD11A1/2 (measured by Terra at ~11:30 and ~22:30) and MYD11A1/2 (measured by Aqua at ~13:30 and ~1:30) have been used. In order to assess which LST products are more suitable in predicting maximum/minimum air temperatures at the global scale, we built two sets of models using both products and compared their performances. As shown in Supplementary Table 9, the regression model built with MOD11A2 outperforms that with MYD11A2, which is consistent with the

previous study by Zhu et al. (32) that also compared the performances of these two products in predicting daily maximum/minimum air temperatures. These performance differences can be explained by observation times and diurnal temperature fluctuations. While the observations of MYD11A are close to maximum/minimum LSTs, the earlier observation times of MOD11A result in daytime LSTs lower than the maximum values and nighttime LSTs higher than the minimum values, resulting in smaller diurnal fluctuations observed by MOD11A than those by MYD11A. Therefore, the fluctuations observed by MOD11A are closer to the fluctuations of ATs, which are usually smaller than LSTs.

Supplementary Figure 8 and Supplementary Figure 9 show the relationships between the observed air temperature and land surface temperature (1st columns), and the predicted air temperature (2nd columns), in summer and winter respectively. Compared to LSTs, the air temperatures predicted by the AT-LST model show stronger correlations with the observed values, with no bias (slope = 1 and intercept = 0).

2.4 Assessing uncertainty propagation

In the SUHI and AT-LST models established above, estimations of coefficients involve ranges of uncertainty (the standard deviations in parentheses in Supplementary Table 7 and Supplementary Table 8). When used in predicting the future intensification of UHI, the uncertainties will propagate through the two models. Since the projected AUHIs are the products of multiplying increases in urban cluster size with the slope in SUHI model (Supplementary Table 7) and then with the slope in AT-LST model (Supplementary Table 8), we can use the multiplication error propagation formula (38) to measure the standard deviation of AUHI increases:

$$\sigma_{\Delta AUHI} \approx |\Delta AUHI| \cdot \sqrt{\left(\frac{\sigma_{slope1}}{slope1}\right)^2 + \left(\frac{\sigma_{slope2}}{slope2}\right)^2}$$

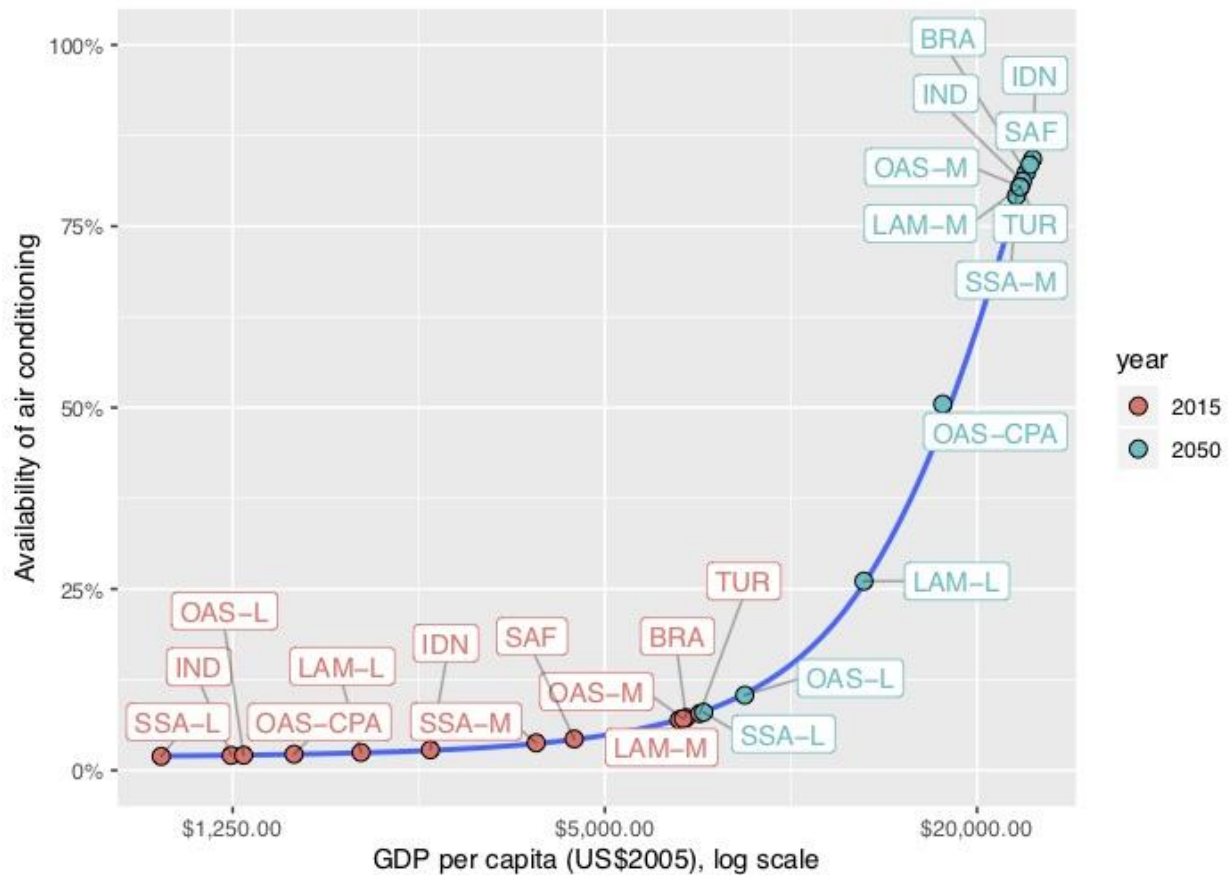
where σ denotes standard deviation, *slope1* is the slope in the SUHI model, and *slope2* is that in the AT-LST model.

2.5 Predicting urban heat island intensification and population exposure

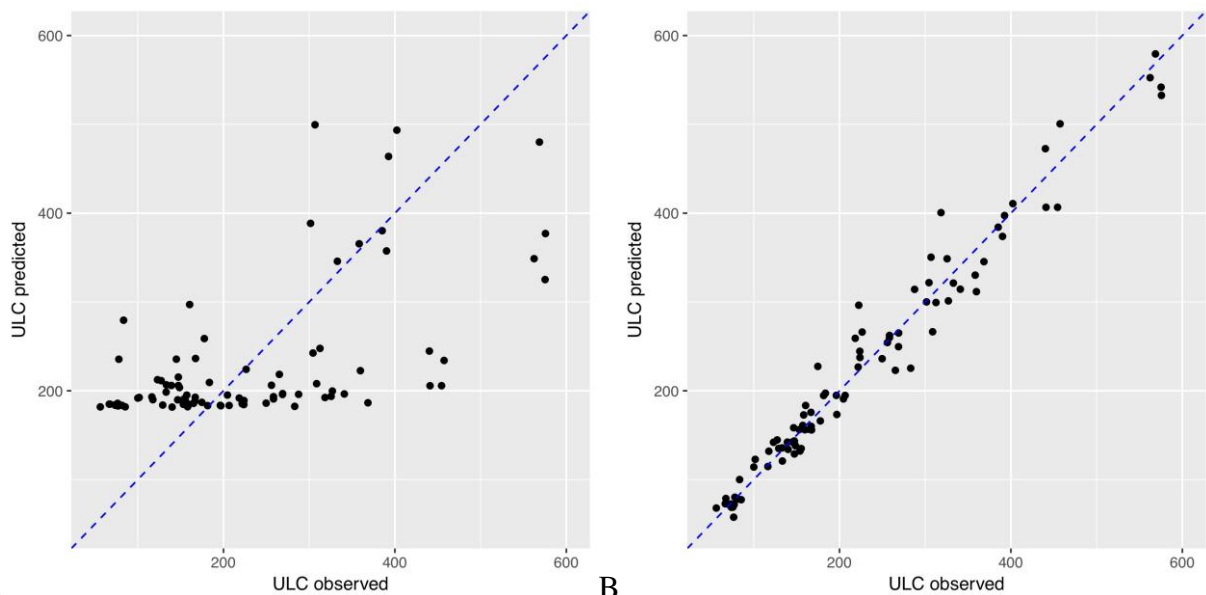
The increased sizes of urban clusters from 2015 to 2050 forecasted in the urban expansion model, are used in the above SUHI model to predict the future increased LST. Apart from urban cluster size, other SUHI determinants stay constant. Within an urban cluster, we allocate the intensification results according to the observed pattern that LST generally decreases from the core to the outer boundary(22). We first divide the cluster into four equal-area concentric rings, then allocate the predicted 75-100th percentiles SUHI to the inner most ring, 50-75th to the second ring, 25-50th to the third, and 0-25th to the outer most one. We then apply the AT-LST model to the resulting increased SUHI to predict future intensification of AUHI.

2.6 Affordability of indoor cooling

The proportion of households with air conditioners (AC) installed depends on climate and on income. While climates determine the needs for AC, incomes determine whether the household can afford to install, maintain, and operate AC. Following a global-scale study(39), we model affordability of indoor cooling as a logistic function of GDP per capita, using the same coefficients listed in the reference.

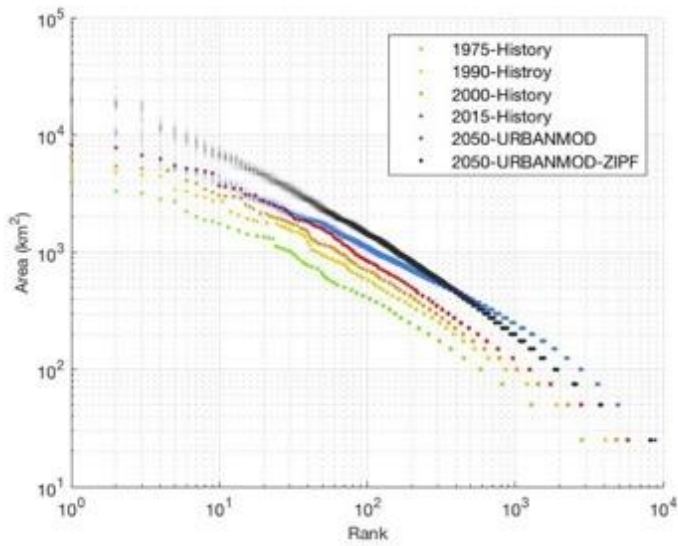


Supplementary Figure 1 Growth of availability of air conditioning from 2015 (red) to 2050 (blue), in the SSP5 scenario. See Supplementary Table 1 for regions definition.



Supplementary Figure 2 Observed versus predicted urban land per capita (ULC) in km^2 per million persons of 32 regions defined in SSP database. A) Predicted by linear regression. B) Predicted by panel data regression. The $y = x$ reference line is dashed blue.

264



265

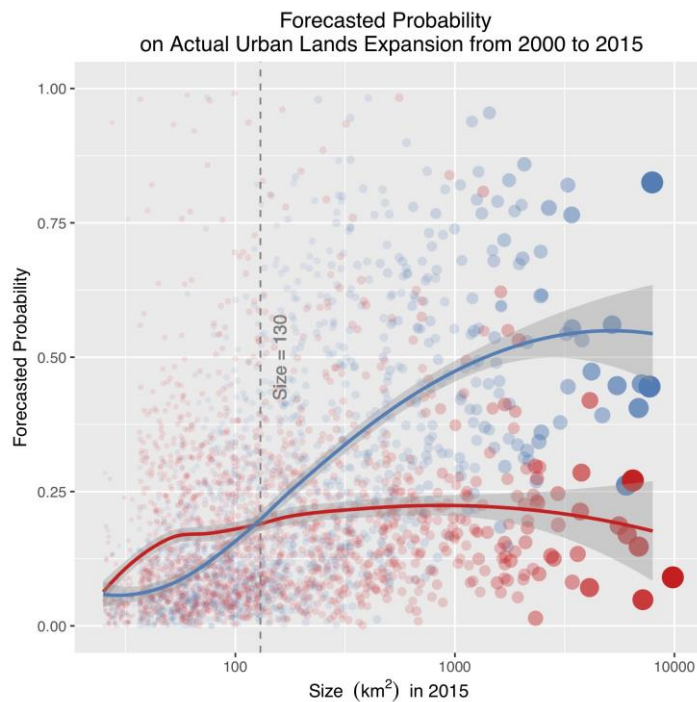
266

267

268

269

Supplementary Figure 3 Rank-Size distributions of global urban areas in 1975 (green), 1990 (yellow), 2000 (orange), and 2015 (red) obtained from Global Human Settlement Layer (GHSL) and those in 2050 under the SSP5 scenario, forecasted by the new model (URBANMOD-ZIPF, black) and the previous model (URBANMOD, blue). Both ranks and sizes are on the logarithmic scale.

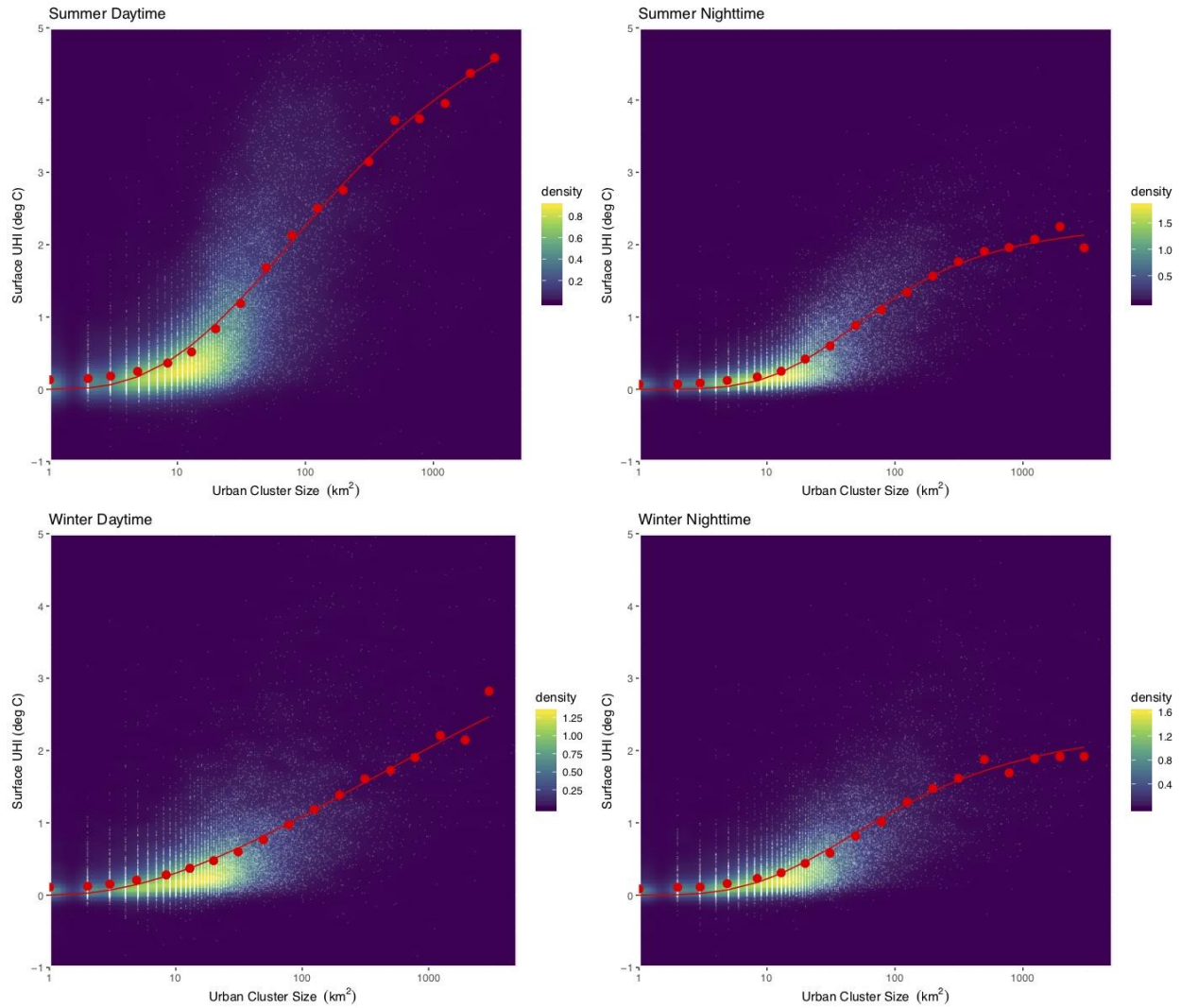


270

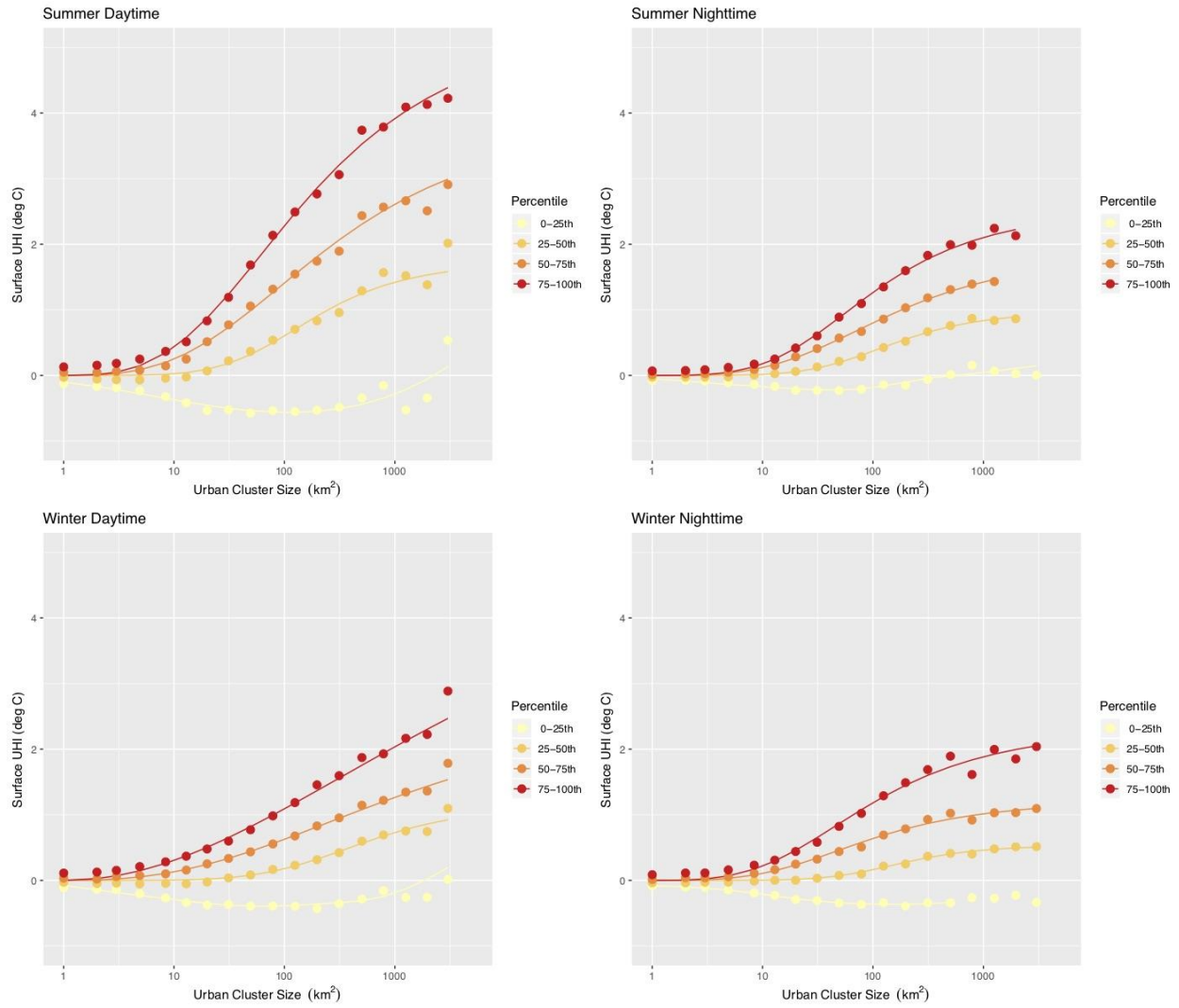
271

272

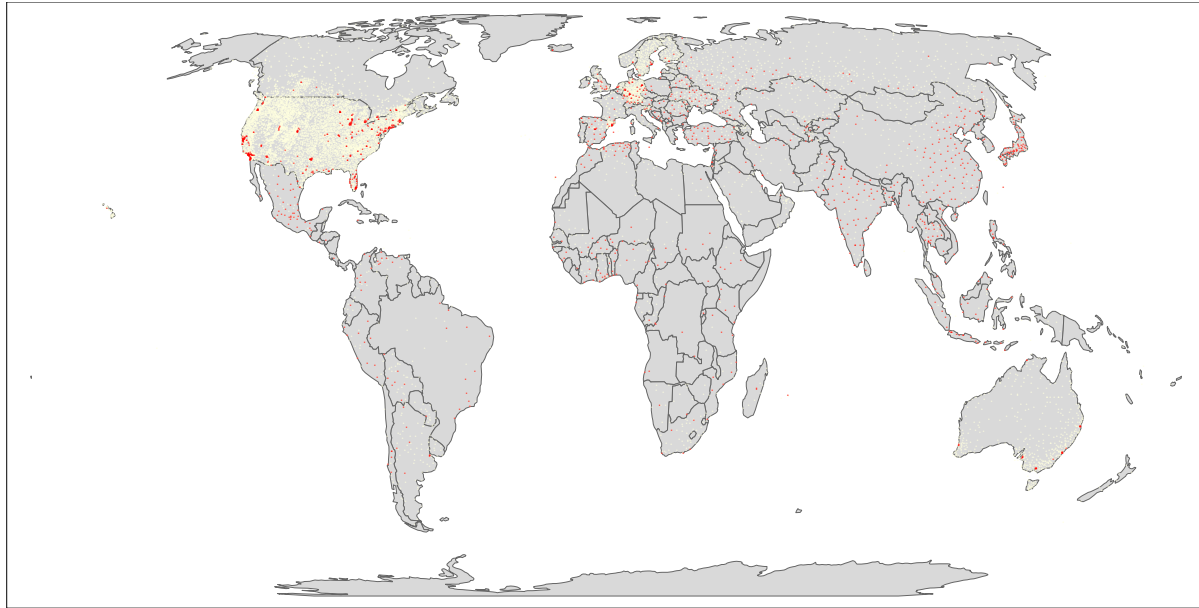
Supplementary Figure 4 Forecasted probabilities of urbanization predicted by URBANMOD-ZIPF (blue) and URBANMOD (red) on the observed new urban lands from 2000 to 2015. Each dot is one urban cluster in 2015.



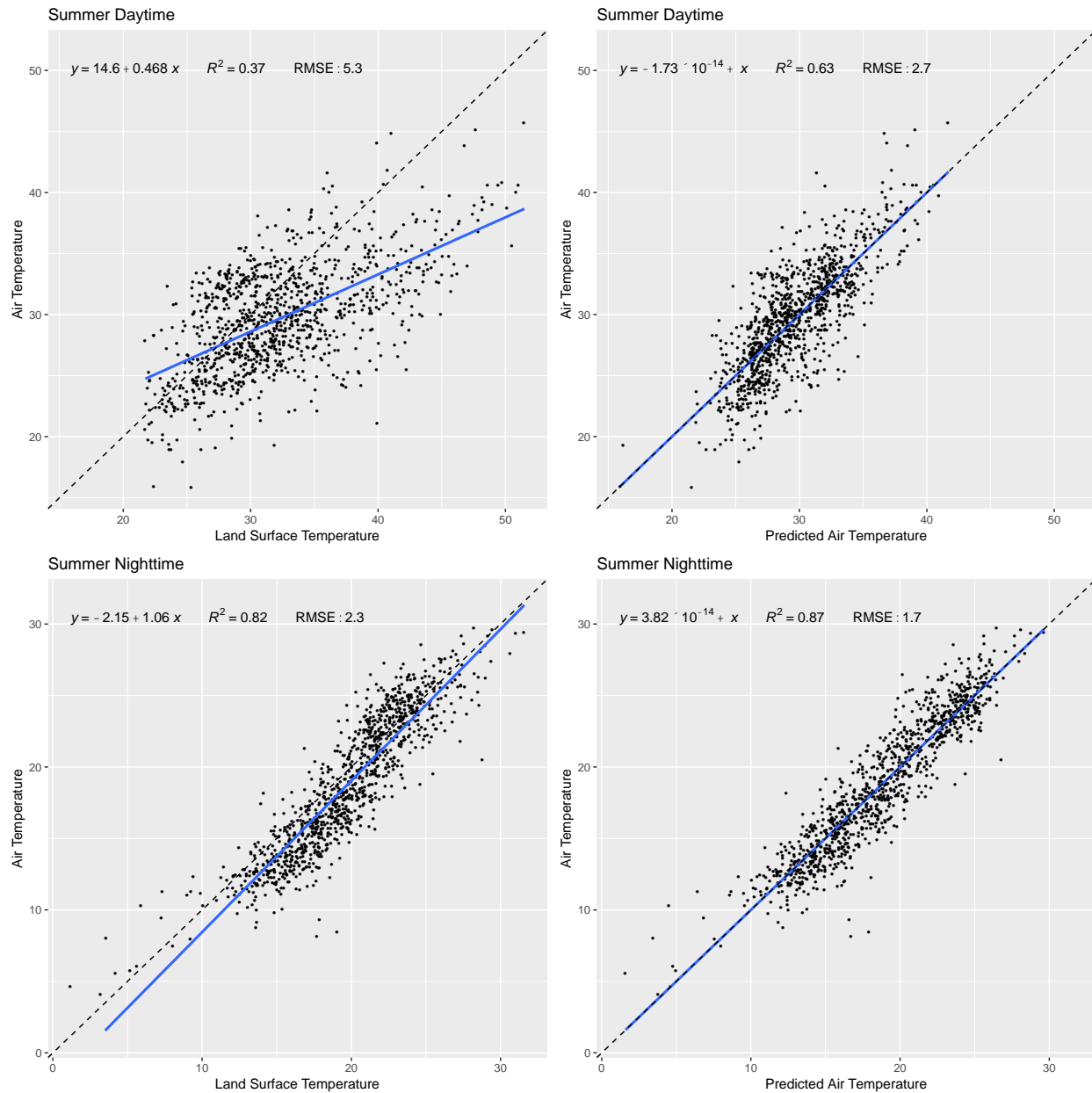
Supplementary Figure 5 Surface UHI intensities (75-100th percentiles) versus urban cluster size. Every white dot represents one urban cluster, and the background colors (dark blue to yellow) represents the density of dots. Red dots present the mean of each bin and the red lines are the fitted Sigmoid functions.



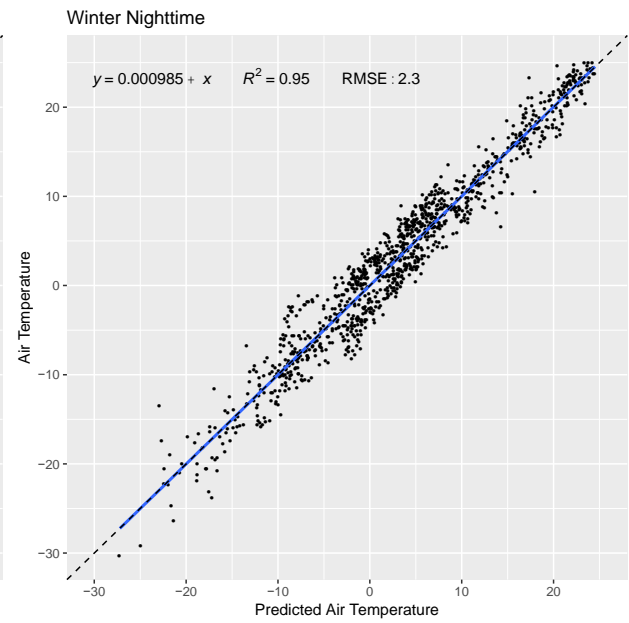
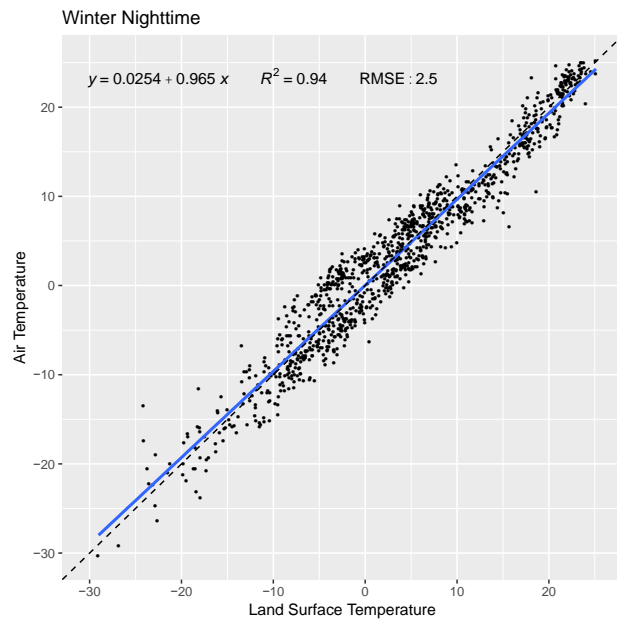
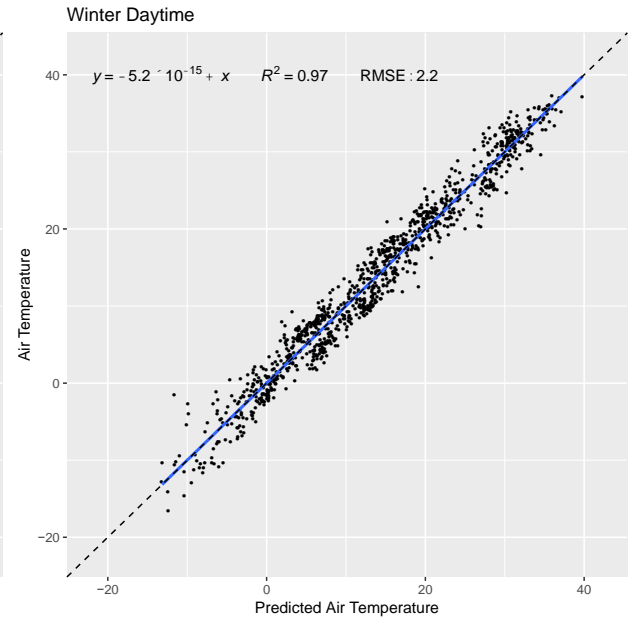
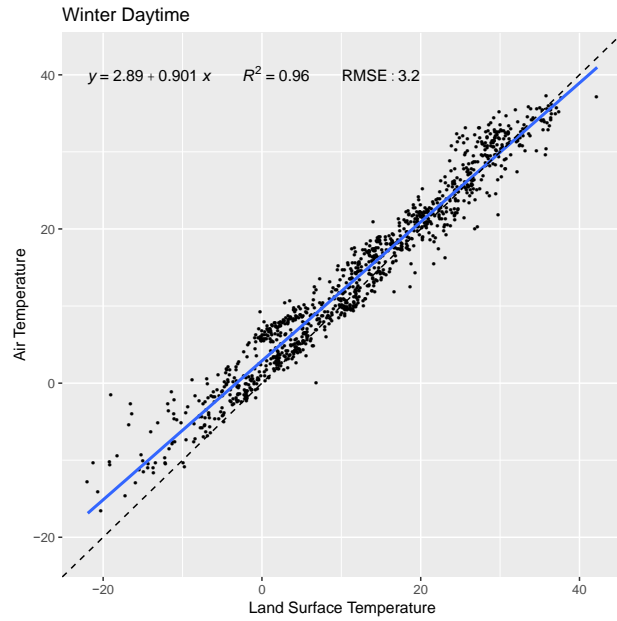
Supplementary Figure 6 The mean SUHIs and cluster sizes of each bin and the fitted curves. Colors present different percentiles of SUHIs.



Supplementary Figure 7 Locations of Global Historical Climate Network (GHCN) weather stations (yellow dot), where urban stations are shown as red dots.



Supplementary Figure 8 Observed air temperature versus land surface temperature and the predicted air temperature in summer. The first column shows the air temperature (y-axis) versus land surface temperature (x-axis), and the second column shows that versus the predicted air temperature (x-axis). The first row shows the summer daytime temperatures, and the second row shows the summer nighttime temperatures. The blue solid lines are linear regression fits. The $y=x$ reference lines are dashed black.



Supplementary Figure 9 Observed air temperature versus land surface temperature and the predicted air temperature in summer. Same as Supplementary Figure 8 but for winter.

Regions	Countries and territories included
ANUZ	Australia, New Zealand
CAN	Canada
EEU	Eastern Europe (excl. former Soviet Union and EU member states): Albania, Bosnia and Herzegovina, Croatia, Montenegro, Serbia, The former Yugoslav Republic of Macedonia
EFTA	Iceland, Norway, Switzerland
EU12-H	New EU member states that joined as of 2004 - high income: Cyprus, Czech Republic, Estonia, Hungary, Malta, Poland, Slovakia, Slovenia
EU12-M	New EU member states that joined as of 2004 - medium income: Bulgaria, Latvia, Lithuania, Romania
EU15	European Union member states that joined prior to 2004: Austria, Belgium, Denmark, Finland, France, Germany, Greece, Ireland, Italy, Luxembourg, Netherlands, Portugal, Spain, Sweden, United Kingdom
JPN	Japan
TUR	Turkey
USA	United States of America, including Puerto Rico, United States Virgin Islands
CAS	Countries of Central Asia: Armenia, Azerbaijan, Georgia, Kazakhstan, Kyrgyzstan, Tajikistan, Turkmenistan, Uzbekistan
EEU-FSU	Eastern Europe, former Soviet Union (excl. Russia and EU members): Belarus, Republic of Moldova, Ukraine
RUS	Russian Federation
CHN	China (Mainland, Hong Kong, Macao; excl. Taiwan)
IDN	Indonesia
IND	India
KOR	Republic of Korea
OAS-CPA	Countries of Other Asia - former Centrally Planned Asia: Cambodia, Lao People's Democratic Republic, Mongolia, Viet Nam
OAS-L	Countries of Other Asia - low income: Bangladesh, Democratic People's Republic of Korea, Fiji, Micronesia (Fed. States of), Myanmar, Nepal, Papua New Guinea, Philippines, Samoa, Solomon Islands, Timor-Leste, Tonga, Vanuatu
OAS-M	Countries of Other Asia - medium and high income: Bhutan, Brunei Darussalam, French Polynesia, Guam, Malaysia, Maldives, New Caledonia, Singapore, Sri Lanka, Thailand
TWN	Taiwan
MEA-H	Countries of Middle East Asia - high income: Bahrain, Israel, Kuwait, Oman, Qatar, Saudi Arabia, United Arab Emirates
MEA-M	Countries of Middle East Asia - low and medium income: Iran (Islamic Republic of), Iraq, Jordan, Lebanon, Occupied Palestinian Territory, Syrian Arab Republic, Yemen
NAF	Countries of North Africa: Algeria, Egypt, Libyan Arab Jamahiriya, Morocco, Tunisia, Western Sahara
PAK	Pakistan, Afghanistan
SAF	South Africa
SSA-L	Countries of Sub Sahara Africa (excl. South Africa) - low income: Benin, Burkina Faso, Burundi, Cameroon, Cape Verde, Central African Republic, Chad, Comoros, Congo, Côte d'Ivoire, Democratic Republic of the Congo, Djibouti, Eritrea, Ethiopia, Gambia, Ghana, Guinea, Guinea-Bissau, Kenya, Lesotho, Liberia, Madagascar, Malawi, Mali, Mauritania, Mozambique, Niger, Nigeria, Rwanda, Sao Tome and Principe, Senegal, Sierra Leone, Somalia, South Sudan, Sudan, Swaziland, Togo, Uganda, United Republic of Tanzania, Zambia, Zimbabwe
SSA-M	Countries of Sub Sahara Africa (excl. South Africa) - medium and high income: Angola, Botswana, Equatorial Guinea, Gabon, Mauritius, Mayotte, Namibia, Réunion, Seychelles
BRA	Brazil
LAM-L	Countries of Latin America (excl. Brazil, Mexico) - low income: Belize, Guatemala, Haiti, Honduras, Nicaragua
LAM-M	Countries of Latin America (excl. Brazil, Mexico) - medium and high income: Antigua and Barbuda, Argentina, Bahamas, Barbados, Bermuda, Bolivia (Plurinational State of), Chile, Colombia, Costa Rica, Cuba, Dominica, Dominican Republic, Ecuador, El Salvador, French Guiana, Grenada, Guadeloupe, Guyana, Jamaica, Martinique, Netherlands Antilles, Panama, Paraguay, Peru, Saint Kitts and Nevis, Saint Lucia, Saint Vincent and the Grenadines, Suriname, Trinidad and Tobago, Uruguay, Venezuela (Bolivarian Republic of)
MEX	Mexico

Variable	Estimate	Std. Error	t value	Pr(> t)
GDP	0.0037516	0.0011784	3.2	<0.01
dummy: ANUZ (baseline)	476.3	21.0	13.4	<0.001
dummy: BRA	-345.6	20.1	-9.5	<0.001
dummy: CAN	-182.6	21.1	-5.9	<0.001
dummy: CAS	-242.6	20.6	-6.1	<0.001
dummy: CHN	-304.1	21.2	-8.0	<0.001
dummy: EEU	-218.6	19.7	-6.3	<0.001
dummy: EEU-FSU	-133.6	19.2	-2.8	<0.01
dummy: EFTA	-207.4	19.3	-6.4	<0.001
dummy: EU12-H	-183.7	25.5	-3.2	<0.01
dummy: EU12-M	-169.1	19.0	-3.3	<0.01
dummy: EU15	-229.9	18.0	-5.9	<0.001
dummy: IDN	-251.7	21.2	-4.8	<0.001
dummy: IND	-408.9	22.0	-11.3	<0.001
dummy: JPN	-270.4	18.9	-5.6	<0.001
dummy: KOR	-421.0	18.5	-12.3	<0.001
dummy: LAM-L	-322.1	20.1	-9.0	<0.001
dummy: LAM-M	-348.7	19.0	-9.4	<0.001
dummy: MEA-H	-345.6	21.5	-10.4	<0.001
dummy: MEA-M	-367.2	22.8	-10.3	<0.001
dummy: MEX	-358.9	19.9	-10.0	<0.001
dummy: NAF	-321.9	22.8	-9.2	<0.001
dummy: OAS-CPA	-342.7	22.2	-9.4	<0.001
dummy: OAS-L	-405.4	22.0	-11.4	<0.001
dummy: OAS-M	-233.6	20.6	-6.3	<0.001
dummy: PAK	-399.5	21.3	-11.1	<0.001
dummy: RUS	-292.1	18.7	-7.5	<0.001
dummy: SAF	-81.1	21.0	-1.3	0.19
dummy: SSA-L	-282.8	21.8	-7.8	<0.001
dummy: SSA-M	-222.3	31.5	-4.9	<0.001
dummy: TUR	-348.6	19.3	-10.0	<0.001
dummy: USA	-32.7	28.6	-0.8	0.44

Supplementary Table 3 Performance by URBANMOD and URBANMOD-ZIPF on the new urban lands from 2000 to 2015.

Model	Mean Predicted Probability	Root Mean Squared Errors of Probability
URBANMOD	0.18	0.50
URBANMOD-ZIPF	0.31	0.41

Supplementary Table 4 Urban land (km²) forecasted by this work and that by Seto et al. 2012 (grey shaded).

	Urban land in 2000	Urban Expansion from 2000 to 2030	Urban land in 2015	Urban Expansion from 2015 to 2050				
				SSP1	SSP2	SSP3	SSP4	SSP5
Africa	41,450	303,813	84,853	198,402	169,889	131,724	240,323	206,042
America	224,025	356,323	218,285	208,998	199,791	145,461	168,746	274,447
Asia	225,825	903,529	249,256	545,259	431,489	285,207	436,483	612,774
Europe	151,075	115,118	198,952	136,113	110,462	25,931	90,861	189,509
Oceania	10,450	12,871	12,663	18,591	17,808	8,336	16,283	26,526
World	652,825	1,691,654	764,009	1,107,363	929,440	596,658	952,696	1,309,297

Supplementary Table 5 Correlations between urban cluster size, its sigmoid index, and different types of SUHIs.

Time of day	Season	SUHIs by percentiles	R ² with $\log_{10}(\text{size})$	R ² with $S(\log_{10}(\text{size}))$	Improvement of R ²
Daytime	Summer	75-100 th	0.46	0.51	10.8%
		50-75 th	0.32	0.36	12.5%
		25-50 th	0.15	0.18	20.0%
	Winter	75-100 th	0.30	0.34	13.3%
		50-75 th	0.19	0.22	15.8%
		25-50 th	0.07	0.10	42.9%
Nighttime	Summer	75-100 th	0.49	0.56	14.3%
		50-75 th	0.38	0.43	13.2%
		25-50 th	0.21	0.26	23.8%
	Winter	75-100 th	0.42	0.47	11.9%
		50-75 th	0.26	0.28	8.7%
		25-50 th	0.06	0.08	33.3%

Supplementary Table 6 Summary of the best subset regressions between SUHIs (75-100th percentiles) and the determinants. The sign 'X' denotes that the determinant is included in the regressions, and the percentage in the parenthesis is the marginal contribution to the final coefficients of determination (R^2).

Time of day	Season	$S(\log_{10}(\text{size}))$	EVI	Elevation	Albedo	Compactness	Roughness	NTL	R^2
Daytime	Summer	X (80%)							0.51
		X	X (14%)						0.60
		X	X	X (3%)					0.62
		X	X	X	X (2%)				0.63
		X	X	X	X			X (2%)	0.64
		X	X	X	X	X (<1%)		X	0.64
	Winter	X (79%)							0.34
		X		X (14%)					0.40
		X	X (2%)	X					0.41
		X	X	X	X (2%)				0.42
		X	X	X	X		X (2%)		0.43
		X	X	X	X	X (<1%)	X		0.43
Nighttime	Summer	X (88%)							0.56
		X						X (5%)	0.59
		X		X (3%)				X	0.61
		X	X (3%)	X				X	0.63
		X	X	X			X (2%)	X	0.64
		X	X	X		X (<1%)	X	X	0.64
	Winter	X (94%)							0.47
		X					X (2%)		0.48
		X			X (2%)		X		0.49
		X		X (2%)	X		X		0.50
		X		X	X	X (<1%)	X		0.50

Supplementary Table 7 Summary of the conditional linear regressions of SUHIs of different percentile ranges (75-100th, 50-75th, and 25-50th). The regressions are conditioned on the background climates (arid, cold, temperate and tropical). The standard errors of the coefficient estimations are shown in the parentheses.

Time of day	Season	Percentiles	R^2	Slope of sigmoid size index $S(\log_{10}(\text{size}))$			
				Arid	Cold	Temperate	Tropical
Daytime	Summer	75-100 th	0.76***	0.34 (± 0.02) ***	0.91 (± 0.04) ***	0.68 (± 0.02) *	0.57 (± 0.03) ***
		50-75 th	0.74***	-0.12 (± 0.03) ***	0.97 (± 0.05) ***	0.63 (± 0.04) ***	0.44 (± 0.04) ***
		25-50 th	0.70***	-0.54 (± 0.04) ***	1.15 (± 0.07) ***	0.60 (± 0.04) ***	0.51 (± 0.05) ***
	Winter	75-100 th	0.76***	0.28 (± 0.03) ***	0.25 (± 0.05) *	0.65 (± 0.04) ***	0.96 (± 0.04) ***
		50-75 th	0.73***	-0.08 (± 0.04) ***	0.31 (± 0.06) ***	0.59 (± 0.04) ***	0.68 (± 0.05) ***
		25-50 th	0.71***	-0.31 (± 0.04) ***	0.51 (± 0.07) ***	0.46 (± 0.05) ***	0.64 (± 0.05) ***
	Summer	75-100 th	0.73***	0.28 (± 0.03) ***	0.25 (± 0.05) *	0.65 (± 0.04) ***	0.96 (± 0.04) ***
		50-75 th	0.71***	-0.08 (± 0.04) *	0.31 (± 0.06) ***	0.59 (± 0.04) ***	0.68 (± 0.05) ***
		25-50 th	0.69***	-0.31 (± 0.04) ***	0.51 (± 0.07) ***	0.46 (± 0.05) ***	0.64 (± 0.05) ***
Nighttime	Winter	75-100 th	0.54***	1.10 (± 0.03) ***	0.95 (± 0.06) ***	0.86 (± 0.04) ***	0.79 (± 0.04) ***
		50-75 th	0.47***	0.73 (± 0.04) ***	0.94 (± 0.08) **	0.74 (± 0.05) *	0.55 (± 0.06) ***
		25-50 th	0.42***	0.46 (± 0.06) ***	1.07 (± 0.10) ***	0.61 (± 0.07) *	0.29 (± 0.08) *

P \leq 0.05*, P \leq 0.01**, P \leq 0.001***

Supplementary Table 8 Summary of the conditional linear regression models of air temperature. The regressions are conditioned on the background climates (arid, cold, temperate and tropical). The standard errors of the coefficients are shown in the parentheses.

Time of day	Season	R ²	Slope of LST			
			Arid	Cold	Temperate	Tropical
Daytime	Summer	0.63***	0.43 (±0.04) ***	0.44 (±0.07) ***	0.44 (±0.05) **	0.30 (±0.08) ***
	Winter	0.87***	0.88 (±0.02) ***	0.69 (±0.03) *	0.69 (±0.06) *	0.85 (±0.02) ***
Nighttime	Summer	0.97***	0.84 (±0.04) ***	0.80 (±0.07) *	0.49 (±0.10) ***	1.04 (±0.05) ***
	Winter	0.95***	0.98 (±0.02) ***	0.88 (±0.04) ***	1.25 (±0.08) ***	0.84 (±0.03) ***

P ≤ 0.05*, P ≤ 0.01**, P ≤ 0.001***

Supplementary Table 9 Summary of the linear regression models of air temperature, with MOD11A2 and MYD11A2 land surface temperature as independent variables.

MODIS data	Time of day	Season	R ²
MYD11A2	Daytime	Summer	0.46***
		Winter	0.54***
	Nighttime	Summer	0.82***
		Winter	0.81***
MOD11A2	Daytime	Summer	0.63***
		Winter	0.87***
	Nighttime	Summer	0.97***
		Winter	0.95***

P ≤ 0.05*, P ≤ 0.01**, P ≤ 0.001***

3 References

- O'Neill BC, et al. (2015) The roads ahead: Narratives for shared socioeconomic pathways describing world futures in the 21st century. *Glob Environ Change*. doi:10.1016/j.gloenvcha.2015.01.004.
- IIASA (2013) *IIASA Shared Socioeconomic Pathways (SSP) database* Available at: <https://tntcat.iiasa.ac.at/SspDb/dsd?Action=htmlpage&page=about>.
- Seto KC, Güneralp B, Hutyrá LR (2012) Global forecasts of urban expansion to 2030 and direct impacts on biodiversity and carbon pools. *Proc Natl Acad Sci* 109(40):16083–16088.
- Gabaix X (1999) Zipf's Law for Cities: An Explanation. *Q J Econ* 114(3):739–767.
- Oke TR (1973) City size and the urban heat island. *Atmospheric Environ* 1967 7(8):769–779.
- Zhou B, Rybski D, Kropp JP (2013) On the statistics of urban heat island intensity. *Geophys Res Lett* 40(20):5486–5491.
- Tan M, Li X (2015) Quantifying the effects of settlement size on urban heat islands in fairly uniform geographic areas. *Habitat Int* 49:100–106.

- 341 8. Li X, Zhou Y, Asrar GR, Imhoff M, Li X (2017) The surface urban heat island response to
342 urban expansion: A panel analysis for the conterminous United States. *Sci Total Environ*
343 605–606:426–435.
- 344 9. Pesaresi M, et al. (2013) A Global Human Settlement Layer From Optical HR/VHR RS Data:
345 Concept and First Results. *IEEE J Sel Top Appl Earth Obs Remote Sens* 6(5):2102–2131.
- 346 10. Seto KC, Fragkias M, Güneralp B, Reilly MK (2011) A Meta-Analysis of Global Urban
347 Land Expansion. *PLOS ONE* 6(8):e23777.
- 348 11. Pontius RG, et al. (2008) Comparing the input, output, and validation maps for several
349 models of land change. *Ann Reg Sci* 42(1):11–37.
- 350 12. Giustarini L, et al. (2016) Probabilistic Flood Mapping Using Synthetic Aperture Radar
351 Data. *IEEE Trans Geosci Remote Sens* 54(12):6958–6969.
- 352 13. Weiss DJ, et al. (2014) An effective approach for gap-filling continental scale remotely
353 sensed time-series. *ISPRS J Photogramm Remote Sens* 98:106–118.
- 354 14. Zhou B, Rybski D, Kropp JP (2017) The role of city size and urban form in the surface
355 urban heat island. *Sci Rep* 7(1):4791.
- 356 15. Peng S, et al. (2012) Surface Urban Heat Island Across 419 Global Big Cities. *Environ Sci*
357 *Technol* 46(2):696–703.
- 358 16. Clinton N, Gong P (2013) MODIS detected surface urban heat islands and sinks: Global
359 locations and controls. *Remote Sens Environ* 134:294–304.
- 360 17. Zhang P, Imhoff ML, Wolfe RE, Bounoua L (2010) Characterizing urban heat islands of
361 global settlements using MODIS and nighttime lights products. *Can J Remote Sens*
362 36(3):185–196.
- 363 18. Rozenfeld HD, et al. (2008) Laws of population growth. *Proc Natl Acad Sci*
364 105(48):18702–18707.
- 365 19. Schwarz Nina, Manceur Ameer M. (2015) Analyzing the Influence of Urban Forms on
366 Surface Urban Heat Islands in Europe. *J Urban Plan Dev* 141(3):A4014003.
- 367 20. Zhao L, Lee X, Smith RB, Oleson K (2014) Strong contributions of local background
368 climate to urban heat islands. *Nature* 511(7508):216–219.
- 369 21. Kutner (2013) *Applied Linear Statistical Models 5ed* (Mc Graw Hill India). 5th edition.
- 370 22. Imhoff ML, Zhang P, Wolfe RE, Bounoua L (2010) Remote sensing of the urban heat
371 island effect across biomes in the continental USA. *Remote Sens Environ* 114(3):504–513.
- 372 23. Peel MC, Finlayson BL, McMahon TA (2007) Updated world map of the Köppen-Geiger
373 climate classification. *Hydrol Earth Syst Sci Discuss* 4(2):439–473.

- 374 24. Rasul A, Balzter H, Smith C (2015) Spatial variation of the daytime Surface Urban Cool
375 Island during the dry season in Erbil, Iraqi Kurdistan, from Landsat 8. *Urban Clim* 14:176–
376 186.
- 377 25. Rasul A, Balzter H, Smith C (2016) Diurnal and seasonal variation of surface Urban Cool
378 and Heat Islands in the semi-arid city of Erbil, Iraq. *Climate* 4(3). doi:10.3390/cli4030042.
- 379 26. Czajkowski KP, et al. (1997) Biospheric environmental monitoring at BOREAS with
380 AVHRR observations. *J Geophys Res Atmospheres* 102(D24):29651–29662.
- 381 27. Shi L, et al. (2016) Estimating daily air temperature across the Southeastern United States
382 using high-resolution satellite data: A statistical modeling study. *Environ Res* 146:51–58.
- 383 28. Kloog I, Nordio F, Coull BA, Schwartz J (2014) Predicting spatiotemporal mean air
384 temperature using MODIS satellite surface temperature measurements across the
385 Northeastern USA. *Remote Sens Environ* 150:132–139.
- 386 29. Li X, Zhou Y, Asrar GR, Zhu Z (2018) Developing a 1 km resolution daily air temperature
387 dataset for urban and surrounding areas in the conterminous United States. *Remote Sens*
388 *Environ* 215:74–84.
- 389 30. Lin X, et al. (2016) Empirical estimation of near-surface air temperature in China from
390 MODIS LST data by considering physiographic features. *Remote Sens* 8(8).
391 doi:10.3390/rs8080629.
- 392 31. Chen F, Liu Y, Liu Q, Qin F (2015) A statistical method based on remote sensing for the
393 estimation of air temperature in China. *Int J Climatol* 35(8):2131–2143.
- 394 32. Zhu W, Lü A, Jia S (2013) Estimation of daily maximum and minimum air temperature
395 using MODIS land surface temperature products. *Remote Sens Environ* 130:62–73.
- 396 33. Benali A, Carvalho AC, Nunes JP, Carvalhais N, Santos A (2012) Estimating air surface
397 temperature in Portugal using MODIS LST data. *Remote Sens Environ* 124:108–121.
- 398 34. Kloog I, et al. (2016) Modelling spatio-temporally resolved air temperature across the
399 complex geo-climate area of France using satellite-derived land surface temperature data.
400 *Int J Climatol*:n/a-n/a.
- 401 35. Rosenfeld A, et al. (2017) Estimating daily minimum, maximum, and mean near surface air
402 temperature using hybrid satellite models across Israel. *Environ Res* 159:297–312.
- 403 36. Lin S, Moore NJ, Messina JP, DeVisser MH, Wu J (2012) Evaluation of estimating daily
404 maximum and minimum air temperature with MODIS data in east Africa. *Int J Appl Earth*
405 *Obs Geoinformation* 18:128–140.
- 406 37. Menne MJ, Durre I, Vose RS, Gleason BE, Houston TG (2012) An Overview of the Global
407 Historical Climatology Network-Daily Database. *J Atmospheric Ocean Technol* 29(7):897–
408 910.

- 409 38. Clifford AA (1973) *Multivariate Error Analysis : A Handbook of Error Propagation and*
410 *Calculation in Many-Parameter Systems* (Applied Science Publishers Ltd., London). First
411 Edition edition.
- 412 39. Isaac M, van Vuuren DP (2009) Modeling global residential sector energy demand for
413 heating and air conditioning in the context of climate change. *Energy Policy* 37(2):507–
414 521.
- 415